



# IMPLEMENTATION OF DEFOCUSING DPIV AND APPLICATION TO THE BUBBLY FLOW AROUND A PROPELLER

F. Pereira<sup>1</sup>, M. Gharib<sup>1</sup>, D. Modarress<sup>2</sup>, D. Dabiri<sup>1</sup>

**Keywords:** 3D PIV, propeller, bubbles, two-phase flows

## ABSTRACT

*Defocusing digital particle image velocimetry (DDPIV) is the natural extension of digital particle image velocimetry (DPIV), planar or quasi three-dimensional, to a true and unique three-dimensional PIV technique. This work presents the defocusing optical concept by which the depth information can be retrieved, thus overriding the limitation to in-plane measurements of actual PIV techniques, either standard or stereo-based. The concept is implemented into a three-dimensional imaging system specifically designed for the purpose of mapping two-phase bubbly flows. Digital images of the bubble field are recorded and analysed to provide information both on the physical location of every single particle/bubble and on its respective size, which is estimated from the scattered light intensity. The calculation of the true three-component velocity field is done by local spatial cross-correlation between two consecutive sets of particle/bubble locations. The spatial resolution and uncertainty limits are established based on a simplified model of the defocusing optical system. Measurements show that the average error on the particle displacement is less than 0.05 pixel. The methodology used to measure the size is laid out by application of the Mie scattering theory. A DDPIV prototype instrument was fabricated on specific requirements. The instrument records high resolution images of the bubble field and is capable of providing bubble size and bubble location within a cubic foot volume. The technique is applied to the study of the dynamics of sub-millimeter air bubbles in a three-dimensional vortical flow generated by a propeller. Velocity, bubble size distribution and void fraction for these flows are discussed.*

## 1. INTRODUCTION

Air bubbles are created in large quantities in the wake of ocean vessels by propeller cavitation, by surface entrainment through free surface wave breakage by the ship's bow and stern, or by air entrainment in the turbulent boundary layer near the hull. Because of their large acoustical cross sections, they are responsible for the acoustical signature of the wake, which is known to persist for long periods of time. Larger bubbles will rise to the surface within a very short period of time, resulting in a surface slick detectable by radar or by altitude imaging devices [1]. There has been considerable interest in determining the air bubble population, thus resulting in much progress, specially in the area of bubble acoustics

### Authors:

<sup>1</sup>California Institute of Technology, 1200 East California Blvd, Mail Code 301-46 Pasadena CA 91125 - correspondence to Dr F. Pereira: [frisco@caltech.edu](mailto:frisco@caltech.edu)

<sup>2</sup>VioSense Corporation, 2400 Lincoln Avenue, Altadena, CA 91001

[2] and cavitation inception [3]. Nevertheless, the coupling between bubbles and turbulent flows is far from understood. The experimental approaches in free surface water tunnels and tow tanks can provide an insight into the field of bubbly flow dynamics. However, the turbulent, multi-phase and three-dimensional nature of the flow demands experimental capabilities beyond standard single point measurement techniques [4] or planar imaging systems [5,6]. A non-intrusive diagnostic instrument is needed, capable of mapping the surrounding flow field and tracking the spatial and temporal history of bubbles, with sufficient sensitivity to accurately estimate the void fraction, in three dimensions and within a reasonably large volume. Existing three-dimensional techniques such as holography [7], neutron radiography [8], Doppler tomographic imaging [9], particle tracking [10], multilayer particle imaging [11] or scanning particle imaging [12], suffer from extreme complexity, insufficient spatial or temporal resolution, and/or lack of capability to measure both size and velocity data. In this paper, we present an intrinsically three-dimensional imaging system based on the defocusing concept introduced in [13]. This system is capable of real-time imaging of bubbly flows, providing both bubble size and velocity information in three dimensions. In a first part, we describe the defocusing concept. In the second part, we present the accuracy measurements performed to determine the instrument performance, followed by a specific study for the size measurement. Finally, two cases of a vortical flow, generated by a propeller and seeded with sub-millimeter air bubbles, are presented.

## 2. DEFOCUSING CONCEPT

The foundations of the defocusing concept have been established in [13]. We report here the most important aspects in a revised form. For clarity, we will use the term *particle* when referring both to a solid particle and to a bubble.

### 2.1 Principle

A typical 2-D imaging system, consisting of a converging lens and of an aperture, is represented in Fig. 1 to help describe the Defocusing Digital Particle Image Velocimetry (DDPIV) technique. Figure 1a exhibits a point A, located on the object plane (or reference plane), and a point B placed in between this plane and the lens system. Point A appears focused in A', on the image plane (or sensor plane), while B is projected as a blurred image B'. The DDPIV technique uses a mask with two or more apertures shifted away from the optical axis to obtain multiple images from each scattering source, as shown in Fig. 1b. The image shift  $b$  on the image plane, caused by these off-axis apertures, is related to the depth location of the source points, whereas the scattered light intensity combined with the blurredness is used to recover the size information.

### 2.2 Geometric Analysis

A simplified geometric model of a two-aperture defocusing optical arrangement is represented in Fig. 2. The interrogation domain is defined as a cube of side  $a$ , thus a square in the plane. The back face of this cube is on the reference plane which is placed at a distance  $L$  from the lens plane. Let  $d$  be the distance between apertures,  $f$  the focal length of the converging lens and  $l$  the distance from the lens to the image plane. The image plane is materialized by a photosensor (e.g. CCD) of height  $h$ . The physical space is attached to a coordinate system originating in the lens plane, with the  $Z$ -axis on the optical axis of the system. Coordinates in the physical space are designated  $(X, Y, Z)$ . The image coordinate system is simply the  $Z$ -translation of the physical system onto the sensor plane, i.e. at  $Z = -l$ . The coordinates of a pixel on the imaging sensor are given by the pair  $(x, y)$ . Point  $P(X, Y, Z)$  represents a light scattering source such as particle, bubble, point-like dot, etc. For  $Z \neq L$ ,  $P$  is projected onto points  $P'(x', y')$  and  $P''(x'', y'')$ , separated by the distance  $b$ .

# IMPLEMENTATION OF DEFOCUSING DPIV AND APPLICATION TO THE BUBBLY FLOW AROUND A PROPELLER

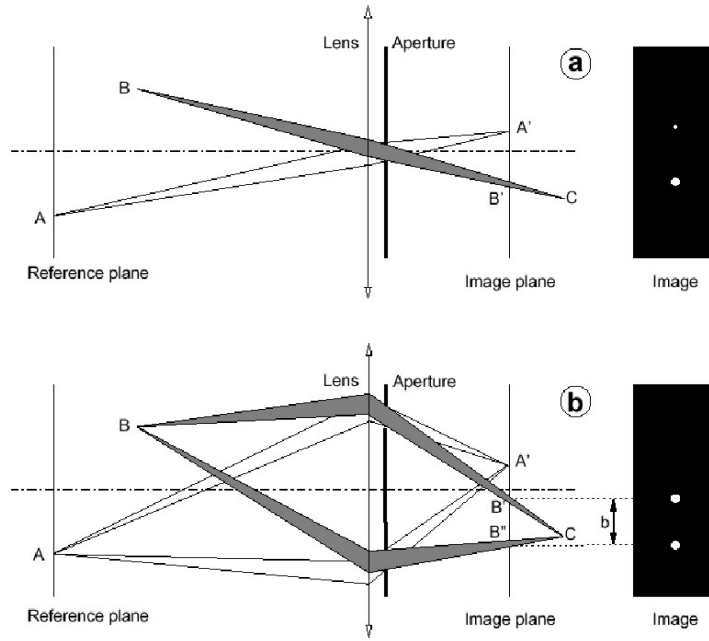


**Fig 1. The defocusing principle: a) standard imaging system, b) defocusing arrangement**

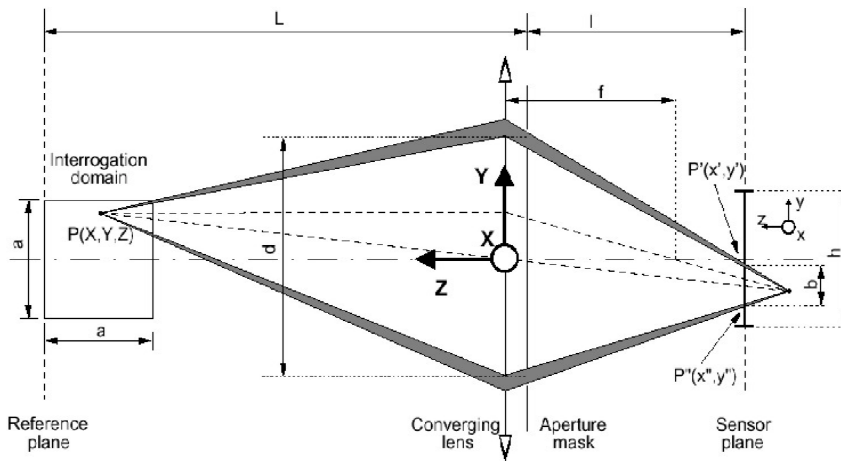


**Fig 2. Simplified defocusing optical model**

### **Image coordinates**

The coordinates  $(x', y')$  and  $(x'', y'')$  of the images  $P'$  and  $P''$  of  $P(X, Y, Z)$  in the image plane are given by the following relations:

$$\begin{cases} x' = x'' = -ML \frac{X}{Z} \\ y' = \frac{M}{2Z} [d(L - Z) - 2LY] \\ y'' = \frac{M}{2Z} [-d(L - Z) - 2LY] \end{cases} \quad (1)$$

where  $M$  is the optical magnification provided by the lens equation.

### **Image separation**

The image separation vector  $\mathbf{b}$  represents the distance between the images  $P'$  and  $P''$ . The norm is therefore given by

$$\begin{aligned}
 b &= \frac{Md}{Z}(L - Z) \\
 &= \frac{1}{K} \left( \frac{1}{Z} - \frac{1}{L} \right) \quad \text{with} \quad K = \frac{1}{MdL}
 \end{aligned}
 \tag{2}$$

The value  $b$  is reported in Fig. 3, nondimensionalized by the height  $h$  of the imaging sensor, as a function of the ration  $Z/L$ . Three values of  $d$  are considered for the aperture separation. The interrogation domain size  $a$  is set to  $100 \text{ mm}$  and the focal plane is such that  $L=1000 \text{ mm}$ . The height of the sensor is  $h=10 \text{ mm}$  (typical for sensors of  $1k \times 1k$  pixels, for instance). The observed domain is defined by a cube whose back face is on the reference plane, but the observable and measurable domain is a volume that extends from the reference plane to a minimum  $Z$  position. This volume encompasses the interrogation domain defined by  $a$ , extending from the focal plane to a point of coordinates  $(0,0,Z_{min})$  on the optical axis where  $b/h$  equals unity, as reported in figure 3.

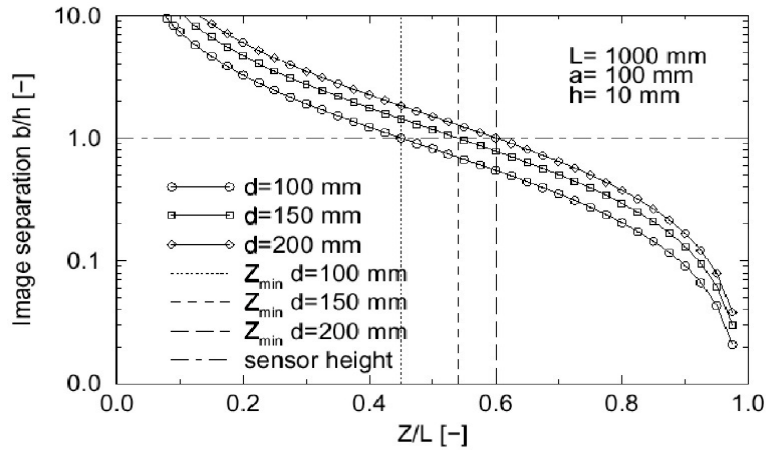


Fig 3. Image separation  $b$

Equation 2 demonstrates the extreme simplicity of the defocusing concept, which of course is greatly valuable in terms of computational implementation and processing speed. In purely geometric terms, the image separation  $b$  is independent of the in-plane coordinates  $X$  and  $Y$ . Likewise, the pinhole diameter has no bearing on  $b$  and is only responsible for the amount of blurredness of any given particle image. It is important to note that these observations are only valid if the system is free of optical aberrations. These aberrations are divided into two classes: focusing aberrations (spherical aberration, astigmatism and coma), which induce magnification errors; image distortion, which creates a nonlinear relationship between the actual location of the particle and its location on the image (i.e. the magnification varies as a function of the position in the field of the image). In particular, increased aberrations are likely to occur with increased separation  $b$ .

From equation 2,  $b$  is negative for  $Z > L$  and reverts sign for  $Z \leq L$ . In other terms, the image pattern defined by the image pair  $P'$  and  $P''$  flips orientation when the object point  $P$  crosses the reference plane. For a two-aperture design as depicted in Fig. 2, this result leads to a non-uniqueness problem because  $b$  is a monotonically decreasing function with increasing  $Z$ : the sign of  $b$  cannot be determined unequivocally from the image information. To overcome this ambiguity, one can either use distinct shapes for the apertures or use multiple apertures. For our prototype instrument, we use three pinholes, arranged into a triangular pattern. This configuration exhibits a flipping triangle when  $P$  moves across the reference plane and requires straightforward and fast image processing routines.

The sensitivity of the system, i.e. its ability to detect small changes of the particle location, can be evaluated through the separation gradient

## IMPLEMENTATION OF DEFOCUSING DPIV AND APPLICATION TO THE BUBBLY FLOW AROUND A PROPELLER

$$\frac{\partial b}{\partial Z} = -\frac{1}{KZ^2} \quad (3)$$

This gradient is reported in Fig. 4 versus  $Z/L$ , for the same values of  $L$ ,  $a$  and  $h$  as above, and for different distances  $d$  between apertures. Because of the nature of  $b$ ,  $\partial b/\partial Z$  increases monotonically with  $Z$  and is independent of the in-plane components, with an asymptotic behavior when approaching the reference plane. The distance  $d$  between the apertures is a critical parameter. Increased  $d$  induces an increased sensitivity of  $b$  on  $Z$  variations, but this has a negative counterpart on the limits of the working domain, which is delimited on one end by the reference plane and on the other end by  $Z_{\min}$ . This value is also reported on the plot for the three values of  $d$  and is seen to approach  $L$  with increasing  $d$ , thus confining the interrogation area to lower sensitivity conditions. However, the separation between apertures should be kept as large as possible for optimum performance.

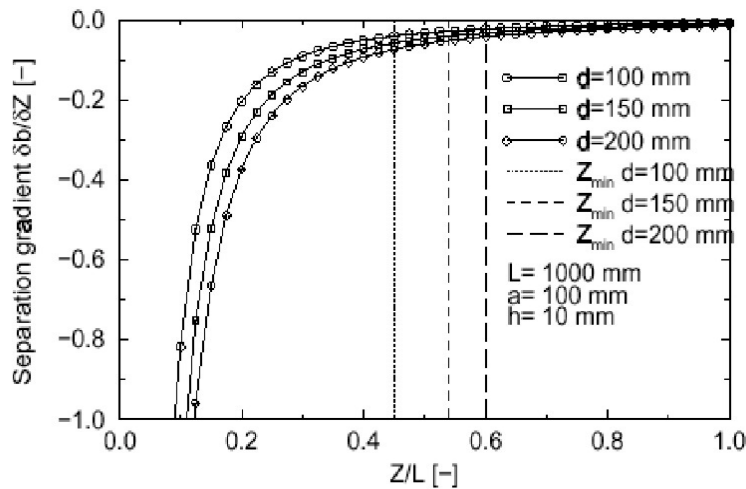


**Fig 4. Image separation gradient**

### *Space coordinates*

The coordinates of  $P$  in the world coordinate system are derived from the image coordinates of the projections  $P'$  and  $P''$ , see equations 1:

$$\begin{cases} X = -\frac{x_0 Z}{ML} & \text{with } x_0 = \frac{x' + x''}{2} \\ Y = -\frac{y_0 Z}{ML} & \text{with } y_0 = \frac{y' + y''}{2} \\ Z = \frac{1}{\frac{1}{L} + Kb} \end{cases} \quad (4)$$

Assuming that the apertures are equidistant from the origin of the coordinate system, the image point defined by  $(x_0, y_0)$  is the image of the particle if there were a single aperture at the origin.

### **2.3 Uncertainty Analysis**

A measure of the overall performance of the system can be defined by considering the ratios between the individual error components, thus giving dimensionless terms that can be used as a comparison criterion between different systems or as a guide criterion in the design stage as to meet the resolution requirements. In PIV techniques, the depth component is derived from in-plane information (i.e. the image). For this reason, the ratio between the out-of-plane and the in-plane error components is a first choice (see e.g. [5]). For the defocusing DPIV

technique, we show using standard errors procedures, that the spatial uncertainties in the object space can be written as

$$\frac{\delta(dZ)}{\delta(dX)} = \frac{\frac{Z}{d}}{\sqrt{\frac{1}{2} + \left(\frac{X}{d}\right)^2}}$$

$$\frac{\delta(dZ)}{\delta(dY)} = \frac{\frac{Z}{d}}{\sqrt{\frac{1}{4} + \left(\frac{Y}{d}\right)^2}} \quad (5)$$

where  $\delta$  is the uncertainty on a given variable.

Let  $e_r$  be the ratio  $\delta(dZ)/\delta(dY)$  defined above. Interestingly, equations 5 show that  $e_r$  depends exclusively on one and only one geometric parameter: the distance  $d$  between apertures.  $e_r$  is reported in Fig. 5 as a function of the off-axis position  $Y/d$  and for different distances  $Z/d$ .  $e_r$  is symmetric about the centerline ( $Y/d=0$ ), where it reaches a maximum value.  $e_r$  falls away from the centre of the field of view.

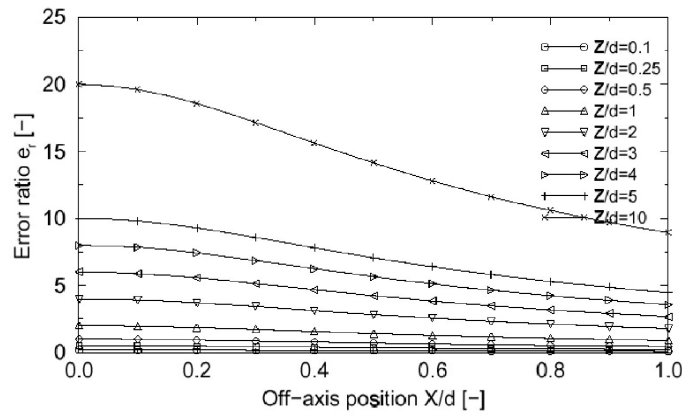


Fig 5. Error ratio  $e_r$  versus off-axis position  $Y/d$  for different distances to camera  $Z/d$

### 3. ACCURACY ASSESSMENT

A camera system has been designed and fabricated based upon the above analysis. The specific characteristics of this instrument can be found in [14]. The DDPIV spatial accuracy and velocity accuracy are addressed hereafter.

#### 3.1 Spatial location

A 12"x12" glass plate with a grid pattern of dots is used and moved along the Z-axis by increments of 10 mm by means of a motorized translation stage. Figure 6 represents, at each station along the Z-axis, the in-plane and out-of-plane mean error and standard deviation, respectively. The average errors on the X-Y plane and on the Z direction are found to be 42  $\mu m$  and 658  $\mu m$ , respectively. With the magnification  $M$ , the in-plane error corresponds in the image plane to 0.08 pixel, whereas the out-of-plane error represents about 1.3 pixels.



## IMPLEMENTATION OF DEFOCUSING DPIV AND APPLICATION TO THE BUBBLY FLOW AROUND A PROPELLER

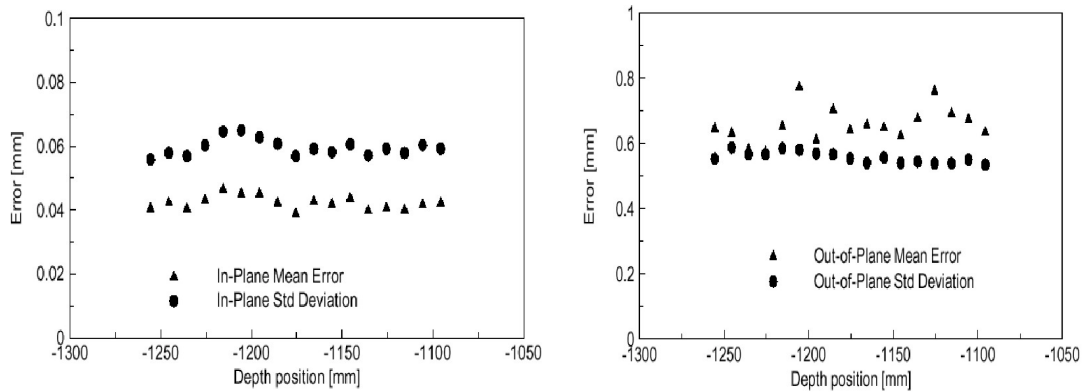


Fig 6. Left: in-plane errors; right: out-of-plane errors

### 3.2 Velocity

The velocity vector field is obtained by local spatial cross-correlation between small volume elements (*voxels*) containing particles observed at two time steps, as described in [14]. The velocity accuracy is established using a flat and rigid disk of  $300\text{ mm}$  in diameter and put into rotation. The disk is tilted in space to cover the full interrogation domain. The tangential velocity is set to  $1\text{ m}\cdot\text{s}^{-1}$  at the outer radius. Figure 7 shows the absolute mean error and the root mean square error on the displacement corresponding to the measured velocity, plotted against the actual displacement. Both are expressed in terms of pixel displacements. The mean error on the displacement is below 0.05 pixel. The *rms* error is found to increase almost linearly with the reference displacement. Indeed, the cross-correlation procedure provides the most probable displacement in any given voxel. Moreover, the computed velocity vector is positioned at the center of the corresponding voxel. For these reasons and because the measurements are performed using a purely rotating flow, the *rms* error increases with the observed displacement.

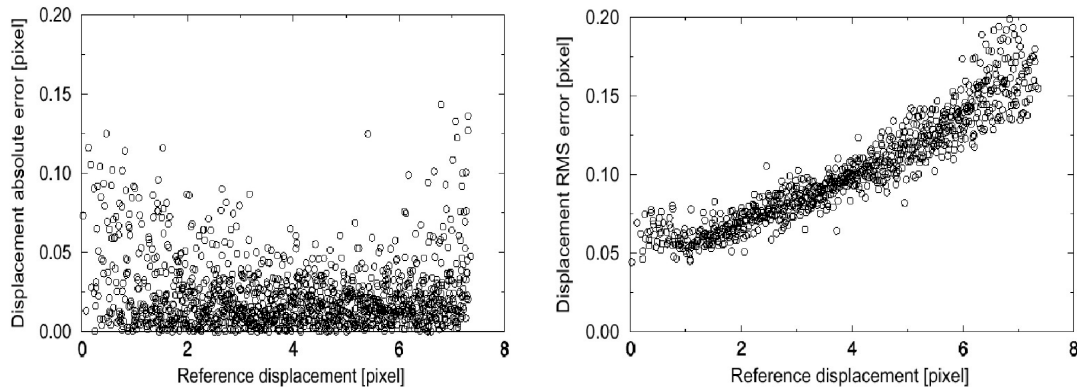


Fig 7. Left: displacement absolute error; right: displacement rms error

## 4. SIZE MEASUREMENT

The Lorenz-Mie theory provides the exact solution to the problem of scattering of light by a single, homogeneous sphere of arbitrary size [15]. This theory relates the particle/bubble scattering intensity to the sphere size. In this study, the size measurement procedure consists of measuring the intensity of the light scattered by calibrated glass microspheres. A matrix of

these microspheres is immersed into a water tank and moved along the camera Z-axis. Let  $I_0$  be a reference intensity value. Figure 8 displays the normalized intensity  $I/I_0$  averaged over all Z positions versus the sphere radius  $a$ . The log-log representation exhibits a power law relationship. The power of the fitting curve ( $\approx 1.92$ ) is found to correspond to the theoretical value of 2 derived from the Mie scattering theory and found experimentally by other researchers [16]. This result suggests that one could use such a relation to make effective and accurate size measurements based on the particle/bubble intensity, provided a reference intensity is available at every location in the interrogation volume. Finally, as one would expect from the spatial accuracy measurements presented earlier, the spatial resolution of the current DDPIV system is here clearly bounded to radii no larger than  $100 \mu\text{m}$ . One can overcome this limit by using higher resolution and higher sensitivity image sensors.

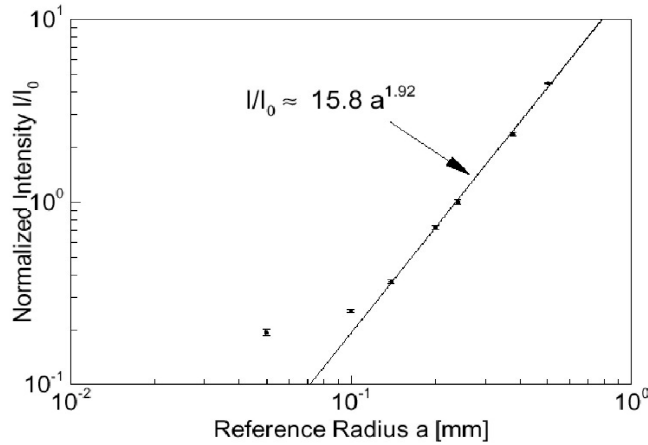


Fig 8. Normalized scattered intensity versus reference radius  $a$  and power fit

## 5. APPLICATIONS

### 5.1 Case 1

A two-blade model boat is immersed into a large water tank. The rotation speed is  $12 \text{ rps}$ , corresponding to a tangential velocity of  $2.52 \text{ m.s}^{-1}$  at the tip of the blades. A bubble generator placed below the propeller produces a dense stream of rising sub-millimeter air bubbles. The 3-D mean velocity field is obtained by phase averaging.

Massless particles are then numerically injected into the mean velocity data set, in a radial arrangement and one diameter upstream of the propeller. Paths of bubbles are determined, providing an unique insight into this complex flow as shown in Fig. 9. Color/gray level relates to the local measured velocity amplitude. Velocity reaches a maximum of  $2.49 \text{ m.s}^{-1}$  in the outer region of the propeller, matching closely the blade tip tangential velocity.



## IMPLEMENTATION OF DEFOCUSING DPIV AND APPLICATION TO THE BUBBLY FLOW AROUND A PROPELLER

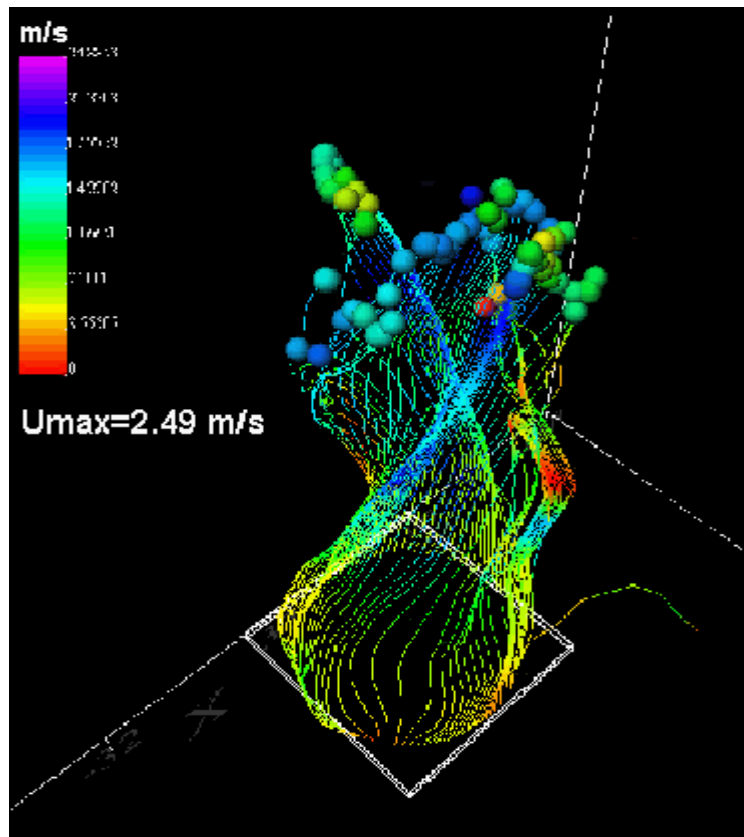


**Fig 9. Pathlines of bubbles around the propeller**

The bubble mean radius along the  $Y$  vertical axis of the flow (rotation axis of the propeller) is reported in Fig. 10. The mean radius increases almost linearly to almost  $325 \mu\text{m}$  at  $Y \approx 30 \text{ mm}$ , where the propeller is located. After the bubbles pass the immediate vicinity of the propeller, the radius is found to follow the opposite trend, decreasing to about  $200 \mu\text{m}$ . The growth of bubbles is partly due, but to a very small extent, to the decrease of the static pressure with increasing  $Y$ . In fact, bubbles experience first the low pressure in the suction side of the propeller before getting into the high pressure region where they collapse.

In the same figure, we report the histograms calculated taking the same bubble population below and above  $Y=30 \text{ mm}$  (about 10000 bubbles in each side). The histogram peak follows the trend outlined before due to the pressure variations. The ratio of the upstream to the downstream populations is 65%. However, the ratio of the respective void fractions ( $V_f$ ) is close to 100%. These observations indicate that coalescence of bubbles is the main mechanism acting here, although breakup may occur in the propeller region. However, these observations only apply to this specific flow. Flows with higher velocities, higher levels of turbulence or where mechanisms of bubble generation are present (e.g. cavitating flows), would show a different behavior.

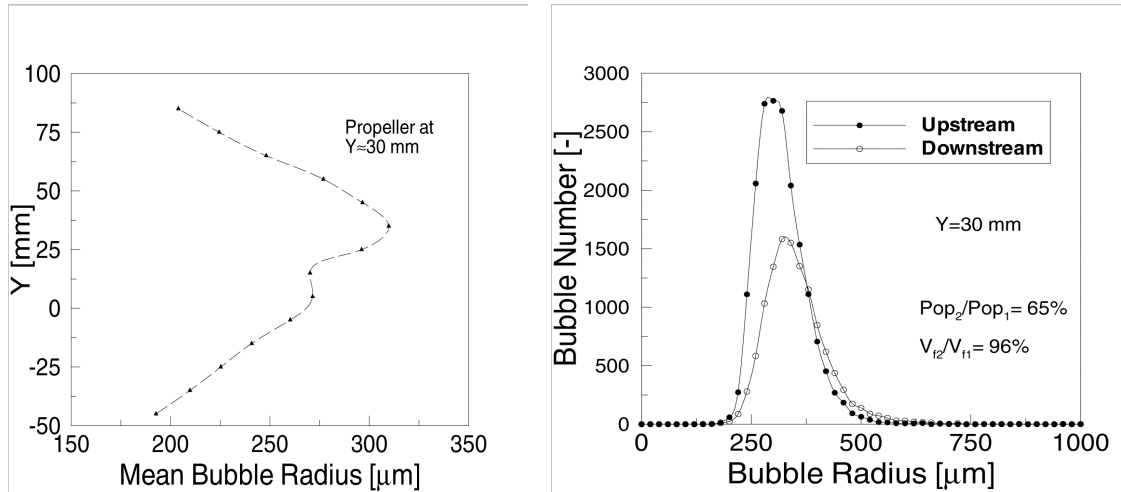


Fig 10. Left: bubble mean radius versus  $Y$ ; right: size distribution upstream and downstream section  $Y=30\text{ mm}$

## 5.2 Case 2

A similar configuration is used here. A three-blade model boat propeller is rotated at  $12\text{ Hz}$ . The velocity field represented in Fig. 11 is obtained by phase-averaging a sequence of 50 instantaneous velocity fields covering a  $200 \times 200 \times 400\text{ mm}^3$  volume. 72963 vectors ( $33 \times 33 \times 67$  voxels) are calculated through the 3D spatial crosscorrelation procedure. Spurious vectors can be seen on borders of the interrogation domain.

A slice in the velocity field, as shown in Fig. 12, clearly displays the high speed jet core along the downstream section of the propeller axis. However, the isovelocity contours displayed on the same figure show a viscous wake that appears as a velocity defect due to the merging of the two boundary layers from the blades. A slight contraction of the slipstream, not illustrated here, could also be detected. The wake is found to rapidly fade into the bulk flow. Presently, work is being performed on every aspect of this flow that should carry out new results, along with interesting comparisons with works from other researchers, e.g. [17,18].

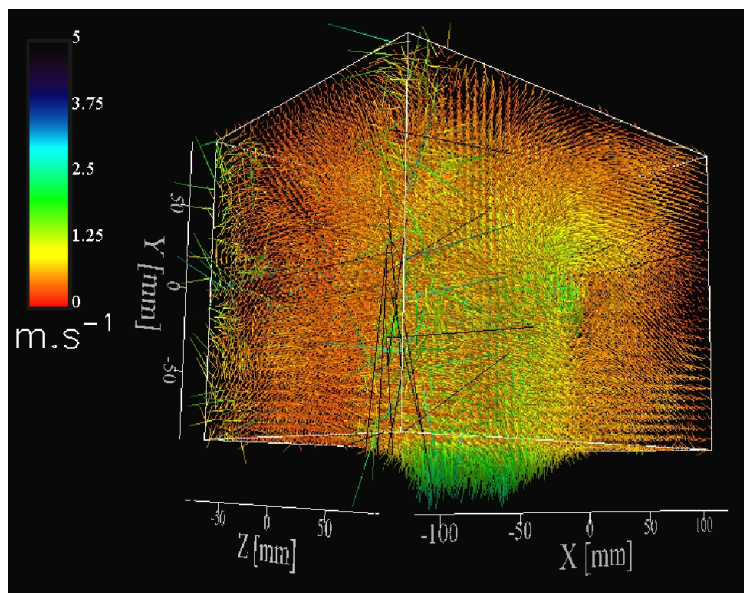


Fig 11. Velocity field:  $200 \times 200 \times 400\text{ mm}^3$ , 72963 vectors ( $33 \times 33 \times 67$  voxels)

## IMPLEMENTATION OF DEFOCUSING DPIV AND APPLICATION TO THE BUBBLY FLOW AROUND A PROPELLER

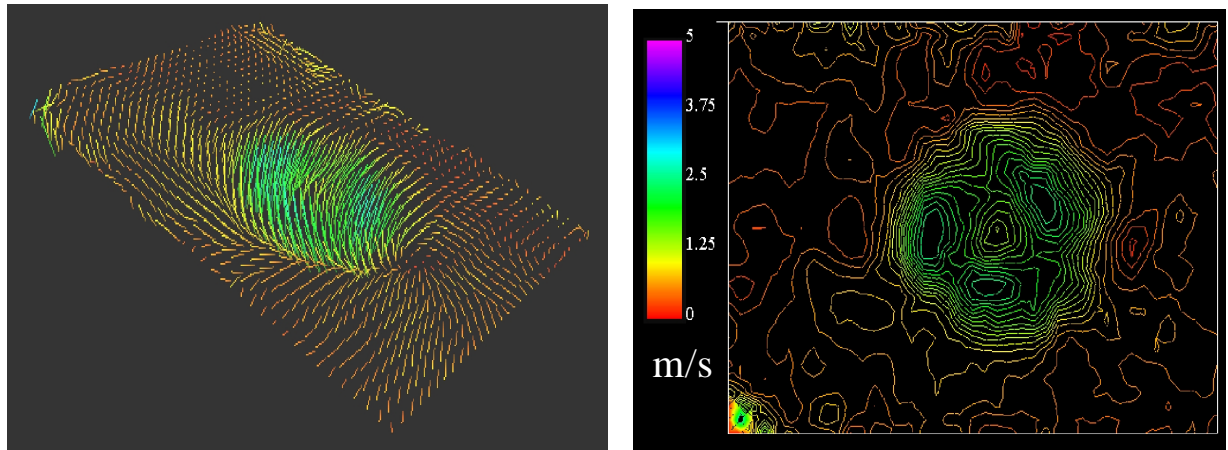


Fig 12. Left: velocity cross-section (downstream region, 0.5 diameter); right: corresponding isovelocity contours

### 6. CONCLUSION AND PERSPECTIVES

The defocusing concept has been analysed, from the geometric point of view and a detailed error analysis has been performed. The prototype instrument designed upon this analysis has an in-plane location error of 0.08 pixel and an out-of-plane location error of 1.3 pixels. In terms of velocity calculation, we found a mean absolute error of less than 0.05 pixel on the displacement evaluation through the three-dimensional spatial cross-correlation procedure. Very encouraging results also show that particle/bubble size can be accurately determined using the scattered light intensity of particles. Good agreement was found with the Mie scattering theory and work is being performed to extend the range of size measurement.

Application to a bubbly flow around a propeller provided an unique insight into this flow. The variations of the mean bubble size were detected as the bubbles were entrained through the propeller. The analysis of the bubble size histograms and of the void fractions upstream and downstream the propeller clearly pointed out that coalescence was the major bubble collective interaction mechanism in this particular flow. In another similar test case, contraction of the slipstream and velocity defect due to the viscous wake were observed.

### ACKNOWLEDGMENTS

The research was supported by the Office of Naval Research (contract N00014-97-1-0303), under the direction of Dr. Edwin P. Rood and Dr. Mark Hyman. The Defocusing Digital Particle Image Velocimetry (DDPIV) technology is protected under a U.S. pending patent filed by California Institute of Technology.

### REFERENCES

- [1] Griffin O. M.; Peltzer R. D., Reed A. M.; Beck R. F.: Remote Sensing of Surface Ship Wakes. *Naval Engineers Journal* pp.245-258, 1995.
- [2] Trevorrow M. V.; Vagle S.; Farmer D. M.: Acoustical Measurements of Microbubbles Within Ship Wakes. *J Acoust Soc Am* 95(4): 1922-1930, 1994.
- [3] Billet M. L.: Cavitation Nuclei Measurements – A Review. *In Proc. Cavitation and Multiphase Flow Forum*, pp. 31-38, Albuquerque, NM, 1985.

- [4] Naqwi A.; Durst F.; Kraft G.: Sizing of Submicrometer Particles Using a Phase-Doppler System. *Applied Optics* 30(33): 4903-4913, 1991.
- [5] Prasad A. K.; Adrian R. J.: Stereoscopic Particle Image Velocimetry Applied to Liquid Flows. *Exp. Fluids* 15:49-60, 1993.
- [6] Grant I.; Fu S.; Pan X.; Wang X.: The Application of an In-line, Stereoscopic, PIV System to 3-Component Velocity Measurements. *Exp. Fluids* 19:214-221, 1995.
- [7] Barnhart D. H. ; Adrian R. J.; Papen G. C.: Phase-Conjugate Holographic System for High-Resolution Particle Image Velocimetry. *Applied Optics* 33(30):7159-7170, 1994.
- [8] Mishima K.; Hibiki T.: Development of High-Frame-rate Neutron Radiography and Quantitative Measurement Method for Multiphase Flow Research. *Nuclear Eng Design* 184: 183-201, 1998.
- [9] Chen Z.; Milner T. E.; Dave D.; Nelson J. S.: Optical Doppler Tomographic Imaging of Fluid Flow Velocity in Highly Scattering Media. *Opt lett* 22: 64-66, 1997.
- [10] Maas H. G.; Gruen A.; Papantoniou D.: Particle Tracking Velocimetry in Three-Dimensional Flows. *Exp Fluids* 15: 133-146, 1993.
- [11] Abe M.; Yoshida N.; Hishida K.; Maeda M.: Multilayer PIV Technique with High Power Pulse Laser Diodes. *In proc. 9<sup>th</sup> Int. Symp. Appl. Laser Tech. Fluid Mech.*, Lisbon, Portugal, 1998.
- [12] Brücker C.: 3D Scanning PIV Applied to an Air Flow in a Motored Engine Using Digital High Speed Video. *Meas Sci Technol* 8: 1480-1492, 1997.
- [13] Willert C. E., Gharib M.: Three-Dimensional Particle Imaging with a Single Camera. *Exp. Fluids*, Vol.. 12, pp 353-358, 1992.
- [14] Pereira F.; Gharib M.; Dabiri D.; Modarress D.: Defocusing DPIV: A 3-Component 3-D DPIV Measurement Technique. Application to Bubbly Flows. Accepted for *Exp Fluids*, 2000.
- [15] Van de Hulst H. C.: *Light Scattering by Small Particles*. Wiley, New York, 1957.
- [16] Landa I.; Tebay E. S.: The Measurement and Instantaneous Display of Bubble Size Distribution, Using Scattered Light. *In Proc. 5<sup>th</sup> Cavitation Forum*, Detroit, MI, 1970.
- [17] Hyun B. S.; Patel V. C.: Measurements in the Flow Around a Marine Propeller at the Stern of an Axisymmetric Body. *Exp Fluids* 11: 33-44, 1991.
- [18] Stella A.; Guj G.; Di Felice F.: Propeller Wake Flowfield Analysis by Means of LDV Phase Sampling Techniques. *Exp Fluids* 28: 1-10, 2000.